






## RESEARCH ARTICLE

# Fine-scale chemostratigraphy of cross-sectioned hydrogenous ferromanganese nodules from the western North Pacific

Shiki Machida<sup>1,2</sup>  | Kentaro Nakamura<sup>3</sup>  | Tetsu Kogiso<sup>4</sup>  |  
Ryo Shimomura<sup>3,2</sup> | Koichi Horinouchi<sup>3,2</sup> | Kyoko Okino<sup>5</sup>  | Yasuhiro Kato<sup>1,2,3</sup> 

<sup>1</sup>Ocean Resources Research Center for Next Generation (ORCeNG), Chiba Institute of Technology, Chiba, Japan

<sup>2</sup>Frontier Research Center for Energy and Resources (FRCER), School of Engineering, The University of Tokyo, Tokyo, Japan

<sup>3</sup>Department of Systems Innovation, School of Engineering, The University of Tokyo, Tokyo, Japan

<sup>4</sup>Graduate School of Human and Environmental Studies, Kyoto University, Kyoto, Japan

<sup>5</sup>Atmosphere and Ocean Research Institute, The University of Tokyo, Tokyo, Japan

## Correspondence

Shiki Machida, Ocean Resources Research Center for Next Generation (ORCeNG), Chiba Institute of Technology, 2-17-1 Tsudanuma, Narashino, Chiba 275-0016, Japan.  
Email: shiki.machida@p.chibakoudai.jp

## Funding information

Japan Society for the Promotion of Science, Grant/Award Numbers: 17H01361, 15H05771; The cross-ministerial Strategic Innovation Promotion Program (SIP) of Japan

## Abstract

A broad area densely covered by ferromanganese nodules was recently discovered around Minamitorishima (Marcus) Island, representing a high-potential metal resource, particularly for Co, Ni, Mo, and W. We studied 16 nodule samples from nodule fields around Minamitorishima Island. To define the fine-scale chemostratigraphy of the nodules, polished cross-sections of the samples were analyzed by microfocus X-ray fluorescence. Our results show that a general pattern of compositional variation was common throughout the growth history of the nodules in all the regions we studied. Chemical mapping clarified changes in the chemical signature and proportion of five lithological components throughout the growth history: Mn represented columnar  $\delta$ -MnO<sub>2</sub>; Fe represented layered amorphous FeOOH·xH<sub>2</sub>O; Ti represented TiO<sub>2</sub>·2H<sub>2</sub>O intergrown with an amorphous FeOOH phase; P, Ca and Y represented particles of biogenic calcium phosphate; and Si, Al, K, Cu, and Ni represented pelagic sediment infills. We proposed a method for creating a multi-dimensional compositional map of the fine-scale chemostratigraphy observed in the ferromanganese oxide layers on the basis of merging the mapped Mn, Fe, Ti, P, Si and Cu intensities. Multi-dimensional compositional mapping of the sampled nodules from the western North Pacific revealed two fundamental findings: (1) previously recognized first-order Fe–Mn layers, L0, L1, and L2, were further divided into two, three, and four sublayers, respectively, and (2) a delayed supply of material to be nuclei of nodule or a growth hiatus of Fe–Mn layer(s), leading to missing sublayers in the layers L0 and L2, regulated the nodule size. In contrast, layer L1, which does not have any missing sublayers, was commonly observed in the samples for this study and has been reported in studies of other regions in the western Pacific. We propose, therefore, that the layer L1 is a key facies for examining chemostratigraphic correlations with other areas of seafloor.

## KEYWORDS

μ-XRF, chemostratigraphy, ferromanganese nodule, Minamitorishima

This is an open access article under the terms of the Creative Commons Attribution-NonCommercial-NoDerivs License, which permits use and distribution in any medium, provided the original work is properly cited, the use is non-commercial and no modifications or adaptations are made.

© 2021 The Authors. Island Arc published by John Wiley & Sons Australia, Ltd.

## 1 | INTRODUCTION

Ferromanganese (Fe–Mn) nodules are polymetallic concretions mainly composed of Fe–Mn (oxyhydr)oxides with significant concentrations of metals, crucial for developing a variety of high-tech and green-tech technologies and devices (Hein et al., 2013; Hein et al., 2020; Petersen et al., 2016). Even though the nodules are found worldwide on deep-sea floors, only recently, a broad area of the field densely covered by hydrogenous Fe–Mn nodules was discovered in the Japanese exclusively economic zone (EEZ) around Minamitorishima (Marcus) Island, hereafter referred to as the Minamitorishima EEZ, in the western North Pacific (Machida et al., 2016; Machida et al., 2019). A geochemical study of nodules collected from the eastern end of the Minamitorishima EEZ (Machida et al., 2016) indicated that they are mainly of hydrogenous origin, and the structure of the Fe–Mn layers, corresponding to compositional changes, are the same as those of the Fe–Mn crust on large seamounts in the Prime Crust Zone (Hein et al., 2009, 2013) in western Pacific. Machida et al. (2016) concluded that these nodules have a high-potential for future metal resource, particularly for Co, Ni, Mo, and W. Moreover, an acoustic survey using a vessel-equipped multiple narrow-beam echo sounder (Machida et al., 2019) defined an approximately 61,200 km<sup>2</sup> region of high backscatter intensity around Minamitorishima Island that corresponds to an area densely covered by hydrogenous Fe–Mn nodules. Therefore, this broad distribution of nodules can demand its development of them as high-potential metal resources.

A study of nodules from the eastern Minamitorishima EEZ (Machida et al., 2016) defined two features of their structure and geochemistry. The large nodules generally consisted of three concentric layers: an outermost sediment-filled mottled layer, L0; a massive black layer, L1; an innermost porous sediment-filled layer, L2. They found that Fe, Ti, and Co were concentrated in the nodule rims compared to the center, and, in contrast, Mn, Al, P, Ca, Ni, and Zn were concentrated in the centers and decreased toward the rims. However, spatial resolution of Fe–Mn oxide layer chemical profiles reported by Machida et al. (2016) was quite low. Moreover, the structural and chemical affinities of nodules distributing in the whole broad nodule fields around Minamitorishima are not confirmed.

Recently, several studies have employed microfocus X-ray fluorescence chemical mapping to visualize either the chemical stratigraphy or micro-fabric of complex multi-phase materials, including Fe–Mn oxide. Spatial resolution of the X-ray mapping vary from 100 to 1  $\mu\text{m}$  (Kashiwabara et al., 2014; Marini et al., 2019; Sipos et al., 2016; Tharalson et al., 2019; Usui et al., 2017) depending on the X-ray source. Particularly, to visualize fine-scale chemical stratigraphy on the cm-sized nodules, an X-ray source with a visual resolution in the order of 100  $\mu\text{m}$  is the most suitable. However, as found in previous studies, it is difficult to investigate compositional correspondence in detail in multipaneled comparisons of several maps of more than two different elements.

To solve the problem, we present a new method for constructing a single map showing multielemental features of Fe–Mn oxide layers by merging several elemental maps constructed via microfocus X-ray

fluorescence analysis. Then, we discuss the chemostratigraphic correlations of nodules collected from different regions around the Minamitorishima Island.

## 2 | GEOLOGICAL BACKGROUND

The Minamitorishima EEZ is located on the northern margin of the Prime Crust Zone (Hein et al., 2009, 2013). Fe–Mn crusts in the Prime Crust Zone are developed on the surface of large seamount slopes. All seamounts in this area are grouped in the West Pacific Seamount Province (WPSP; Koppers et al., 2003; Sager et al., 1993). Seamounts in this region including Minamitorishima Island were formed by the Early–Middle-Cretaceous hotspot volcanism (Aftabuzzaman et al., 2021; Koppers et al., 2003); however, Minamitorishima Island is thought to be overprinted by Paleogene volcanism (Hirano et al., 2021). The oceanic basement below these seamounts, the Cretaceous Pacific Plate, formed between 165 and 157 Ma (Müller et al., 2008; Nakanishi et al., 1989). In the WPSP, Fe–Mn nodules cover a pelagic sediment layer on the abyssal seafloor between the seamounts. The broad area covered densely by nodules in the Minamitorishima EEZ corresponds to an area of a T<sub>1</sub> echo type; an acoustically transparent layer with irregular surface morphology, classified on the basis of acoustic surveys using a sub-bottom profiler (SBP; Nakamura et al., 2016).

The broad area of densely nodules examined in this study was separated into four regions. Region “East EEZ” was located at the eastern end of the Minamitorishima EEZ (Figure 1). Based on an acoustic backscatter intensity map (Machida et al., 2019); we recognized that this region is the northern end of the broad, dense nodule field in the Minamitorishima EEZ. North of the field, thick pelagic sediments are present (Nakamura et al., 2016) containing no or less nodule coverage (Machida et al., 2019). The southern half of the Minamitorishima EEZ was separated into two large basins, the “Southeast EEZ” and “Around Takuyo Daigo Seamount” regions, along the Northern Wake seamount trail (Figure 1). Region “Northeast of EEZ,” isolated from the other three regions and the Prime Crust Zone, was located to the northeast.

## 3 | FIELD OBSERVATION AND SAMPLE SELECTION

Field observations and sample collection were conducted during 10 dives of the submersible *SHINKAI 6500*, 5860–4960-m deep, during the cruises YK10-05, YK16-01, and YK17-11C of the *R/V Yokosuka* in 2010, 2016, and 2017, respectively (Figure 1). The following describes the geology of the dive sites and features of the studied samples in the East EEZ, Southeast EEZ, Around Takuyo Daigo Seamount, and Northeast of EEZ regions in this order. The samples were collected from locations that included the different topographic features of each region. We also describe the results of an acoustic survey in northeast of the EEZ region conducted during cruise YK17-11C of the *R/V Yokosuka*.

### 3.1 | East EEZ region

Two dives of *SHINKAI 6500* (6K#1207 and 6K#1459) were conducted on the same small seamount located approximately 300 km east of Minamitorishima Island, the representative site for this region. As described by Machida et al. (2016), the northwestern ridge and southern slope of the seamount shows high acoustic backscatter intensity and are almost completely covered by well-rounded, 5–10 cm diameter Fe–Mn nodules. Sample 6K#1459N1-006 (Figure S1) was collected from the same site as sample 6K#1207R02 reported by Machida et al. (2016). The sampling site was located on the lower northern flank of the northwestern ridge, corresponding to where the *SHINKAI 6500* landed on the seafloor during both dives. After analyzing both samples, we looked for a correlation between Machida et al.'s (2016) quantitative chemical analysis and the fine-scale chemical mapping conducted in the current study. Sample 6K#1459N3-001 (Figure S1) was collected from a site located on the northwestern ridge. The seafloor facies at both of these sampling sites are classified as Type-V facies (Machida et al., 2019), characterized by almost complete coverage by rounded nodules with a bimodal grain-size distribution. All three samples were classified as large grain-size type (76–101 cm in maximum length; see Table 1) for this region.

### 3.2 | Southeast EEZ region

Three dives of *SHINKAI 6500* (6K#1462, 6K#1463, and 6K#1497) were conducted in the Southeast EEZ region (Figure 1). Site 6K#1462 was located on flat seafloor surrounded by several large seamounts. In contrast, sites 6K#1463 and 6K#1497 were located on gentle slopes at the foot of large seamounts. Samples 6K#1462N3-005, 6K#1462N4-004, 6K#1463N2-002, 6K#1463N3-002, 6K#1497N1-011, and 6K#1497N1-030 (Figure S1) were collected from sampling sites corresponding to Type-H seafloor facies (Machida et al., 2019), consisting of a dense distribution of rounded nodules with a bimodal size distribution. Although most of the selected samples had large grain sizes (63–98 cm in maximum length), to represent each sampling site, samples 6K#1463N3-002 and 6K#1497N1-011 were additionally selected for their smaller grain sizes (55 and 54 cm in maximum length, respectively) to determine the reason for this size differences. The grain sizes of the samples are listed in Table 1.

### 3.3 | Around Takuyo Daigo Seamount region

Machida et al. (2019) found a high acoustic backscatter intensity region quite widely distributed around the Takuyo Daigo Seamount. The regions east and southeast of the Takuyo Daigo Seamount, particularly, exhibited relatively higher acoustic backscatter intensity than other regions and were classified as Type-H or Type-V seafloor facies (Machida et al., 2019). Some small seamounts or knolls are distributed across the flat seafloor in this region (Figure 1).

We conducted four dives of *SHINKAI 6500* (6K#1460, 6K#1464, 6K#1498, and 6K#1499) at different sites covering the following topographic features. Although sites 6K#1460 and 6K#1498 were situated on the flat seafloor east of the Takuyo Daigo Seamount, a small seamount was located near the former site (Figure 1). We selected samples 6K#1460N2-004 and 6K#1498N2-002 as representative of the large-sized rounded nodule (71 and 55 cm in maximum length, respectively) from each site (Figure S1; Table 1). Dive 6K#1464 was conducted on a knoll approximately 50 km southeast of the Takuyo Daigo Seamount (Figure 1). This knoll was surrounded by a moat, so we observed a survey line across the moat. Samples 6K#1464N1-004 and 6K#1464N4-004 (Figure S1) were collected from the bottom of the moat and the shallower outer rim of the moat, respectively. Although the former sample (66 cm in maximum length) was larger than the latter (48 cm in maximum length), as shown in Figure S1 and Table 1, both were representative of each sampling site. In contrast to the other dive sites, the dive 6K#1499 was conducted on the southern slope of the Takuyo Daigo Seamount (Figure 1). Sample 6K#1499N4-004 (Figure S1; Table 1) was collected from a flat terrace on the moderately steep slope, representative of the large grain-size type (67 cm in maximum length) of this sampling site.

### 3.4 | Northeast of EEZ region

The surveyed area was located approximately 100 km northeast of the Minamitorishima EEZ (Figure 1). Based on Japan Coast Guard vessel-equipped multiple narrow-beam echo sounder survey (Figure S2; Oikawa & Morishita, 2009), the region is bounded by a seamount to the west and a seamount chain to the east. Topographic lineament trending northwest–southeast direction with high acoustic backscatter intensity is located in this area. We conducted a stratigraphic survey in the southern part of this region using a vessel-equipped SBP of *R/V Yokosuka*, prior to the *SHINKAI 6500* dive. The profile of the SBP survey (Figure S2) indicate a thin sedimentary layer covering the topographic lineaments (in the northeastern section of the survey line) in contrast to the southwest part of the survey line that has low acoustic reflectivity. The stratigraphic feature of the topographic lineaments corresponds to  $T_1$ -type of facies—an acoustically transparent layer with irregular surface morphology—as obtained in the Japanese EEZ around Minamitorishima Island by Nakamura et al. (2016). The acoustic backscatter intensity was remarkably higher on the top of the lineaments than that at the foot of the lineaments (Figure S2b).

For detailed observations using the *SHINKAI 6500* (6K#1500), we selected a topographic lineament exhibiting the highest backscatter intensity and thinnest sediment layer among in this region (Figure S2). The survey line of the *SHINKAI 6500* corresponds almost to the survey line of the vessel-equipped SBP. Along the survey line of dive 6K#1500, although the nodule density was variable (Figure S3), the seafloor facies was classified as Type-H, as proposed by Machida et al. (2019). Samples 6K#1500N2-002 and 6K#1500N5-003 (Figure S1; Table 1) were collected from the bottom and top of the

topographic lineament, respectively, as the representative large grain-size type (95 and 105 cm in maximum length, respectively) of the sampling site.

## 4 | METHODS

To clarify the compositional structure (chemostratigraphy) for the entire ferromanganese nodule, we performed elemental imaging using microfocus X-ray fluorescence ( $\mu$ -XRF). In contrast to the analysis of thin section(s) using an electron microprobe analyzer, a nondestructive analysis of large samples is the principal advantage of  $\mu$ -XRF. Because Fe–Mn oxide is very brittle, the sample gets severely damaged upon by cutting during thin-section making. Thus, we decided that all the collected samples were cut in half using rock saw, and analyze the surface of the cross-sectioned samples via  $\mu$ -XRF.

The sample sawing was conducted after X-ray Computed Tomography (CT) scanning (Shimomura et al., 2018) to create a

representative cross-section for each sample. The underside (sediment side) of the nodule was recognized on the basis of sediment-attachment on the surface, and the vertical and horizontal directions of sample were determined on the basis of their original position on the seafloor. Then, all the samples were cut vertically except for sample 6K#1462N4-004. CT scanning for the horizontally cut sample 6K#1462N4-004 confirmed that this cross-section covered all the recognized layers. The sample 6K#1207R02 was already cut owing to compositional analysis by Machida et al. (2016). Therefore, the representability of the cross-sectioned sample 6K#1207R02 was confirmed by CT scanning. Subsequently, the cut surface was ground with a 120- $\mu$ m diamond disc to eliminate sawing scuff, followed by polishing with a 70- $\mu$ m diamond disc. Finally, the polished samples were allowed to dry naturally in a well-ventilated place for up to 1 week.

The  $\mu$ -XRF analysis was conducted at Kyoto University. The intensities of Al, Ca, Cu, Fe, K, Mg, Mn, Ni, P, Si and Ti were determined by an energy-dispersive X-ray spectrometer (EDS) attached to a  $\mu$ -XRF spectroscopy (XGT7000V; Horiba, Kyoto, Japan). Multiple

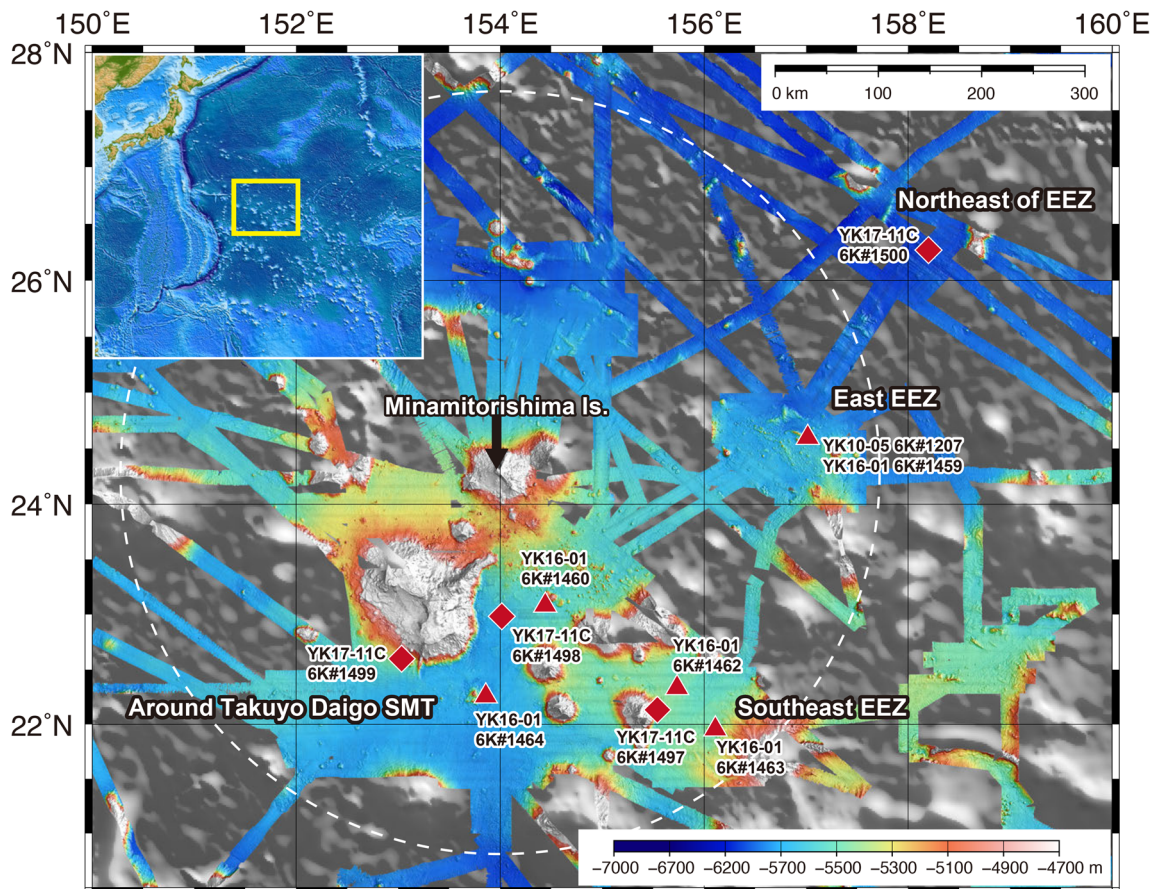


**FIGURE 1** Topography around Minamitorishima Island. The mapped area is indicated in the yellow box in the index map on the upper left-hand corner. The red triangles indicate the locations of the sampling sites (submersible *SHINKAI 6500* dive sites) during the cruises YK10-05 and YK16-01 of the *R/V Yokosuka*. The red diamonds indicate the locations of the sampling sites (submersible *SHINKAI 6500* dive sites) during the cruise YK17-11C of the *R/V Yokosuka*. The colored fine-scale topographic data of a vessel-equipped multiple narrow-beam echo sounder (MBES) were compiled with previous datasets obtained by Machida et al. (2019) and during the cruises MR16-07 of the *R/V Mirai* and YK17-11C of the *R/V Yokosuka*. Topographic data for the gray background of the main map and the map in the upper left-hand corner are from ETOPO1 (NOAA National Geophysical Data Center; <https://www.ngdc.noaa.gov/mgg/global/>). The white dashed line indicates the Japanese exclusive economic zone around Minamitorishima Island

**TABLE 1** Summary of sampling sites, collected ferromanganese nodule samples, and parameters for  $\mu$ -XRF analysis

Cruise	Dive no.	Sample name	Location			Sample size			Analysis parameters				Total analysis time (ms/pixel)
			Latitude (N)	Longitude (E)	Depth (m)	X (mm)	Y (mm)	Z (mm)	X (mm)	Y (mm)	Pixel size ( $\mu$ m)		
YK10-05	6K#1207	6K#1207-R02	24°35.74'	157°00.99'	-5503	100	90	70	94.208	87.032	184	83	
YK16-01	6K#1459	6K#1459N1-006	24°35.69'	157°00.96'	-5501	76	61	56	76.800	59.400	150	99	
YK16-01	6K#1459	6K#1459N3-001	24°33.63'	156°59.66'	-5590	101	75	62	99.328	63.244	194	178	
YK16-01	6K#1460	6K#1460N2-004	23°04.95'	154°25.36'	-5547	71	64	51	69.632	53.312	136	100	
YK16-01	6K#1462	6K#1462N3-005	22°18.90'	155°43.12'	-5455	91	75	60	75.776	55.500	148	94	
YK16-01	6K#1462	6K#1462N4-004	22°18.34'	155°42.49'	-5444	98	84	64	90.112	90.112	176	114	
YK16-01	6K#1463	6K#1463N2-002	21°57.10'	156°06.77'	-5457	67	65	63	68.608	67.356	134	117	
YK16-01	6K#1463	6K#1463N3-002	21°56.85'	156°07.82'	-5271	55	54	53	58.368	58.368	114	76	
YK16-01	6K#1464	6K#1464N1-004	22°15.45'	153°51.38'	-5778	66	61	54	60.416	57.348	118	88	
YK16-01	6K#1464	6K#1464N4-004	22°14.77'	153°53.17'	-5750	48	47	42	47.104	44.068	92	122	
YK17-11C	6K#1497	6K#1497N1-011	22°07.88'	155°32.51'	-5159	54	50	48	51.200	46.100	100	76	
YK17-11C	6K#1497	6K#1497N1-030	22°07.88'	155°32.51'	-5159	63	61	59	63.488	61.380	124	87	
YK17-11C	6K#1498	6K#1498N2-002	22°57.97'	154°00.51'	-5639	55	50	44	50.176	49.196	98	78	
YK17-11C	6K#1499	6K#1499N4-004	22°38.60'	153°02.18'	-4959	67	63	61	67.584	63.492	132	81	
YK17-11C	6K#1500	6K#1500N2-002	24°48.63'	157°02.80'	-5860	95	76	57	97.280	68.780	190	108	
YK17-11C	6K#1500	6K#1500N5-003	24°47.59'	157°01.55'	-5826	105	88	60	80.384	56.834	157	108	

measurements were made using a tube voltage of 50 kV, a tube current of 0.9 A, and an X-ray beam of 100  $\mu\text{m}$  in vacuo. The samples were scanned in approximately 92–194  $\mu\text{m}$  intervals (pixel size) depending on the range of the mapping area (Table 1). Intensity was determined from the cumulative intensity of the repeated analyses (more than 10 times and up to 15 times), with a total analysis time of 76–178 ms/pixel (Table 1). The analysis results were outputted to TIFF-formatted files using the instrument's operation program. The analysis of the elemental maps was conducted using the Image J program (<https://imagej.nih.gov/ij/index.html>).

## 5 | RESULTS AND DISCUSSION

### 5.1 | General features of the elemental maps

To recognize the general features of each elemental intensity map, we initially focused on sample 6K#1207R02 (Figure 2) and the geochemical data reported by Machida et al. (2016). The most identifiable feature is that the Fe is concentrated in the nodule rim rather than the center, in contrast to the Mn being concentrated in the center and decreasing toward the rim, as indicated by the previous chemical analysis (Machida et al., 2016). The Ti is layered and corresponds to the concentrated Fe layers. However, our  $\mu\text{-XRF}$  mapping indicates high-Ti-intensity zones clearly in parts of the layers independent of Fe content, which indicates that the Ti enrichment occurs independently. Multiple spots of high intensity of P, Ca, and Y were mainly observed in the inner Mn-enriched area of the nodule. The Si distribution matched that of the Al and K, infilling the Fe and Mn framework. Area of high-intensity Cu and Ni were presented not only as thin layers in the outer layers but also correlated with Si, Al, and K in the inner layers. Although these correspondences of Al, K, P, Ca, Y, and Cu with Mn were previously recognized by Machida et al. (2016), fine-scale structural nature was clarified by the  $\mu\text{-XRF}$  mapping. The general chemostratigraphical features of sample 6K#1207R02 from the East EEZ region were commonly observed in all the samples collected from the entire of Minamitorishima EEZ (Figure 3; Figures S4–S18).

As shown in Figures 2 and 3, the Mn concentration exhibits a columnar structure of  $\delta\text{-MnO}_2$ . In contrast, the Fe exhibits a layered structure (except in the inner part around a nuclei) and is anti-correlated with Mn, representing amorphous  $\text{FeOOH}\cdot x\text{H}_2\text{O}$ , as was previously recognized (Aplin & Cronan, 1985a, 1985b; Burns & Burns, 1979; Calvert & Price, 1977). The Ti is concentrated with Fe, so that consistent with the affinity of Ti and Fe (i.e.,  $\text{TiO}_2\cdot 2\text{H}_2\text{O}$  intergrown with an amorphous FeOOH phase) defined by leaching experiments (Koschinsky & Halbach, 1995). Small particles of biogenic calcium phosphates (BCP) in deep-sea pelagic sediment highly contain rare-earth element including Y (Fujinaga et al., 2016; Iijima et al., 2016; Kashiwabara, Toda, et al., 2014; Kashiwabara et al., 2018; Kato et al., 2011; Liao et al., 2019; Ohta et al., 2016, 2020; Takaya et al., 2018; Yasukawa et al., 2014). Therefore, we consider that high P, Ca, and Y spots in the nodule indicate the existence of BCP particles. The Si distribution matched that of the Al and K, infilling the

Fe and Mn framework. Si, Al, K, Cu, and Ni were concentrated on the surface of the underside (sediment side) of the nodule. Therefore, we consider that sedimentary materials (i.e., clay minerals) had enriched these elements, representing the existence of and different proportions of sediment infill, as observed by Machida et al. (2016). The results of X-ray diffraction analysis for the sample 6K#1463N3-001 (Figure 4) show that the peaks of  $\delta\text{-MnO}_2$  (Vernadite), quartz, and feldspar are visible in all layers, and no other minerals (phases) are identified. This indicates that other expected phases, such as  $\text{FeOOH}\cdot x\text{H}_2\text{O}$ ,  $\text{TiO}_2\cdot 2\text{H}_2\text{O}$ , and BCP, are amorphous. These results strongly support our interpretation of mapping results and the results of previous studies.

As shown in Figure 3, the outermost Fe-enriched layer appeared thinner in the nodules sampled from the two southern regions (i.e., Southeast EEZ and Around Takuyo Daigo Seamount) than the samples from the East EEZ region. Moreover, area containing particles of BCP were inconsistently associated with Mn-enriched layers. However, we were unable to objectively constrain these observations because several elemental maps were compared. Thus, we propose constructing a multichemical feature map to investigate the chemostratigraphical history in detail by identifying common stratigraphic layers, as discussed in Section 5.2.

### 5.2 | Method for creating a multichemical feature map

As described in Section 5.1, the intensity of each element corresponded to a lithological component comprising the Fe–Mn nodule layers. Fe, Mn, and Ti exhibited characteristic distributions throughout the growth history of the nodules. In contrast, the elemental groups of Ca–P–Y, Si–Al–K, and Cu–Ni share the same concentration features. Here, we thus posited Fe, Mn, Ti, P, Si, and Cu as representative elements for characterizing the chemostratigraphic features. Histograms for each of these representative elements in large-sized samples representing the four regions are shown in Figure 5. They indicate that the frequency distribution of each element was similar for the different regions except for Fe. The frequency distribution of Fe was slightly variable; for example, the irregular single peak of sample 6K#1207R02 and the broad bimodal peak of sample 6K#1500N5-003. This similar chemostratigraphy support a common general growth history for all nodules across the entire Minamitorishima EEZ region; therefore, we are able to adjust the observed X-ray intensity using the same criteria for each representative element, and objectively create a compositional map to visually identify the chemostratigraphic features.

The multichemical feature map was constructed using Image J. Each black and white Fe, Mn, Ti, P, Si, and Cu intensity map was assigned to a colored channel: green, magenta, cyan, yellow, gray, and blue, respectively. They were then merged into a multi-colored map. The level of each element in the merged image was then adjusted on the basis of the following strategy. First, for Ti and Mn, the Window was minimized and the Level was shifted to match the line with the peak of the histogram, followed by the raising of the Window to match

the maximum and minimum of the histogram (i.e., the width of the intensity distribution was matched with the width of the Window). Reducing the Level to match the minimum of the Window to the peak (Figure 5) only improved the visualization of the Ti layering. Second, for P and Cu, the Window was minimized and the Level increased to remove the noise from P (i.e., only the highest P intensity is shown),

and the Level increased to place the line in the middle of the intensity distribution for Cu (i.e., to visualize lower Cu intensity than for the other elements). The Fe signals were optimized by only shifting the Level after adjusting for all the elements except for Si. The Si signals should be minimized to improve the visualization of the fundamental Fe–Mn oxide layer features and any other elemental stratigraphy. However, we

East EEZ: YK05-10 6K#1207R02

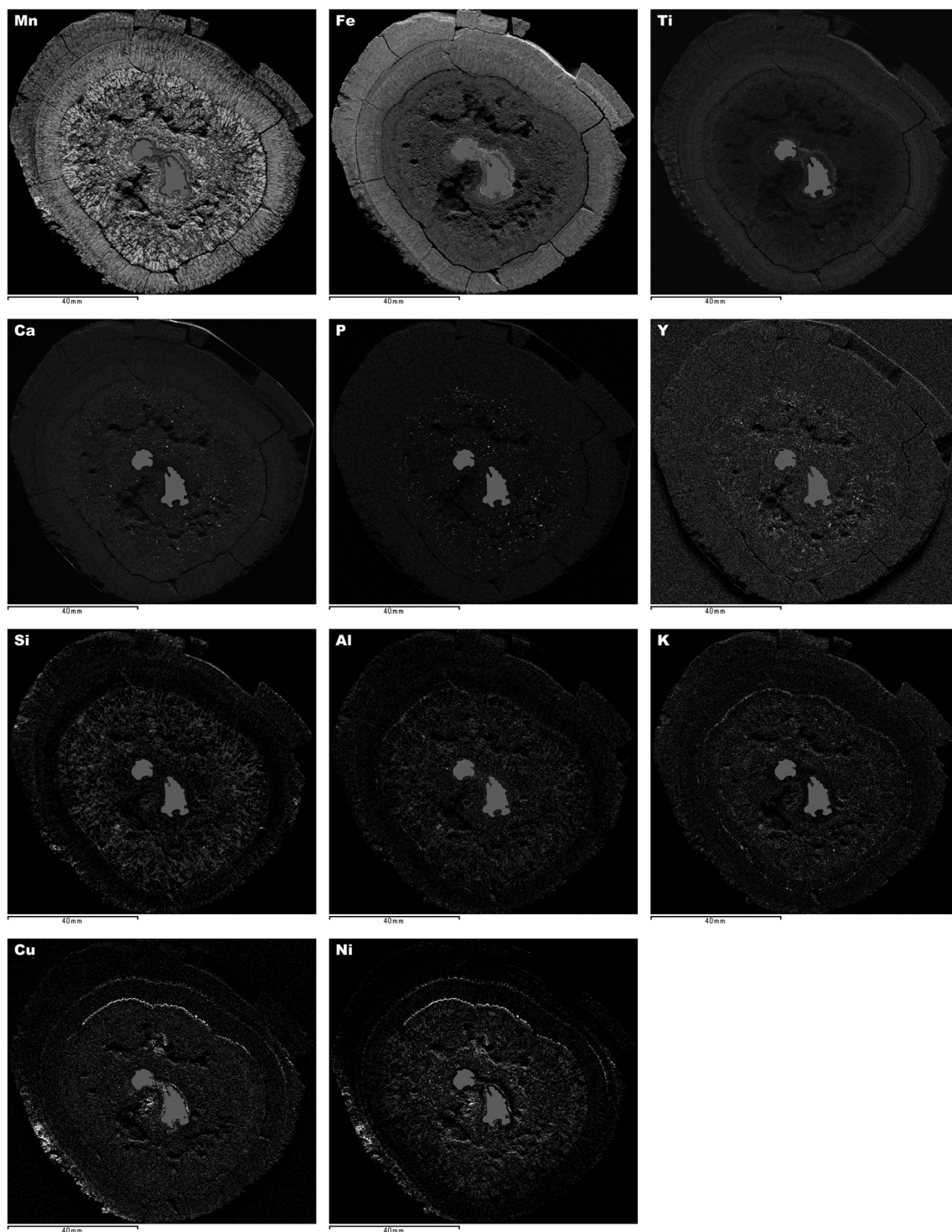
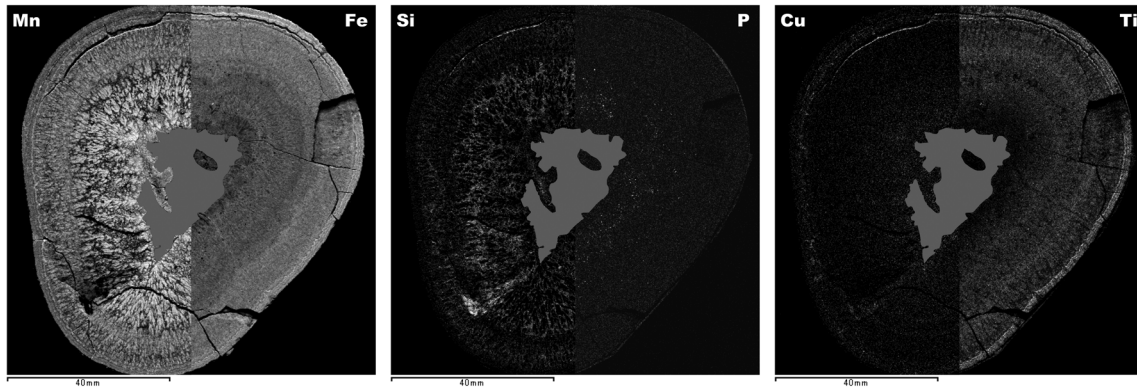
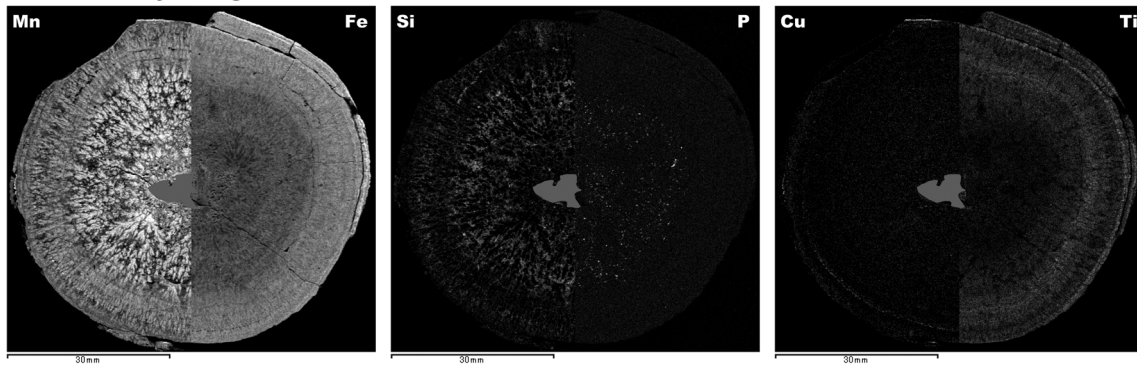


**FIGURE 2** Results of the  $\mu$ -XRF mapping analysis of sample 6K#1207R02 collected from the East EEZ region. The gray field indicates the nuclei of this sample

## Southeast EEZ YK16-01 6K#1462N4-004



## Around Takuyo Daigo SMT YK17-11C 6K#1499N4-004



## Northeast of EEZ YK17-11C 6K#1500N5-003

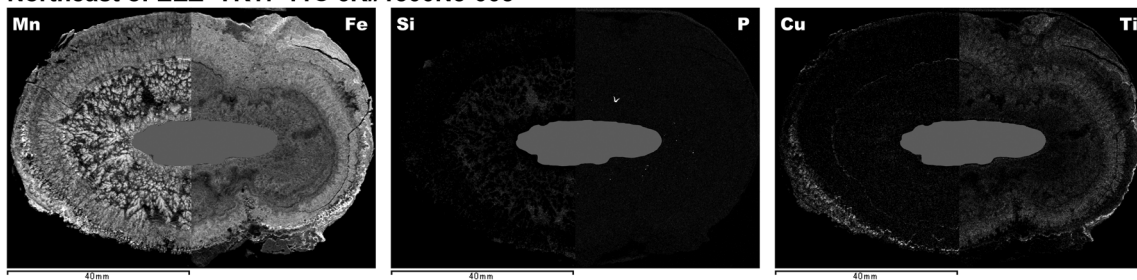


**FIGURE 3** X-ray intensity maps of representative samples for Mn, Fe, Ti, P, Si, and Cu for the Southeast EEZ, Around Takuyo Daigo Seamount, and Northeast of EEZ regions. The gray field indicates the nuclei of this sample

note that the presence of sedimentary materials infilling the Fe and Mn frameworks were easily recognized in the merged map.

The maps for each element obtained by an EDS represent qualitative differences in the intensity of element signals. Because of the different sensitivities of each element, a direct comparison of intensities is not inherently possible. Therefore, it should be noted that the merged map only shows which elements are most characteristic of the individual layers of nodule, even if the map is useful to identify layers.

### 5.3 | Definition of the layers based on the merged map

We defined chemostratigraphic layers on the basis of the merged multichemical feature map. To examine the correlation with lithologically

## YK16-01 6K#1463N3-002

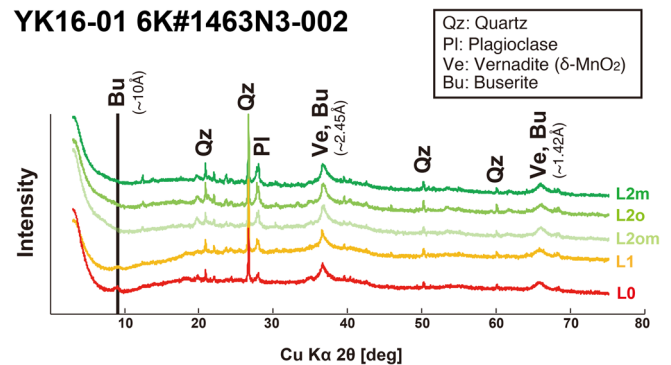


**FIGURE 4** Results of X-ray diffraction analysis for Fe–Mn oxide layers of sample 6K#1463N3-002. Definition of Fe–Mn oxide layers are discussed in the main text and shown in Figure 7. L2m, L2 Middle sublayer; L2o, L2 Outer sublayer; L2om, L2 Outermost sublayer



discriminated layers proposed by Machida et al. (2016), we used sample 6K#1207R02 as a reference, as in Section 5.2. The first-order criteria used to divide the Fe–Mn oxide layers were Fe, Mn, and Ti (Figure 6). We identified three concentric layers corresponding to those proposed by Machida et al. (2016): the outermost Fe-enriched layer corresponded to the mottled sediment-filled layer L0; the intermediate layer, exhibiting high-Ti laminations, corresponded to the massive black layer L1; and the innermost Mn-enriched layer corresponded to the porous layer L2. Layer L1 was also characterized by

lower Si than the other two layers. High Fe in L0 and high Mn in L2 indicated higher and lower Fe/Mn, respectively, as shown Machida et al.'s (2016) compositional analysis.

As shown in Figure 7, the first-order layers, L0, L1, and L2, were respectively subdivided into two, three, and four layers on the basis of a combination of features observed in the Fe, Mn, Ti, P, and Si. The subdivision of L0 and L1 was relatively simple; L0 Inner and L0 Outer were distinguished by a thin low-Si and high-Ti layer. The middle part of L1 exhibited the highest Ti and the lowest Si compositions of the

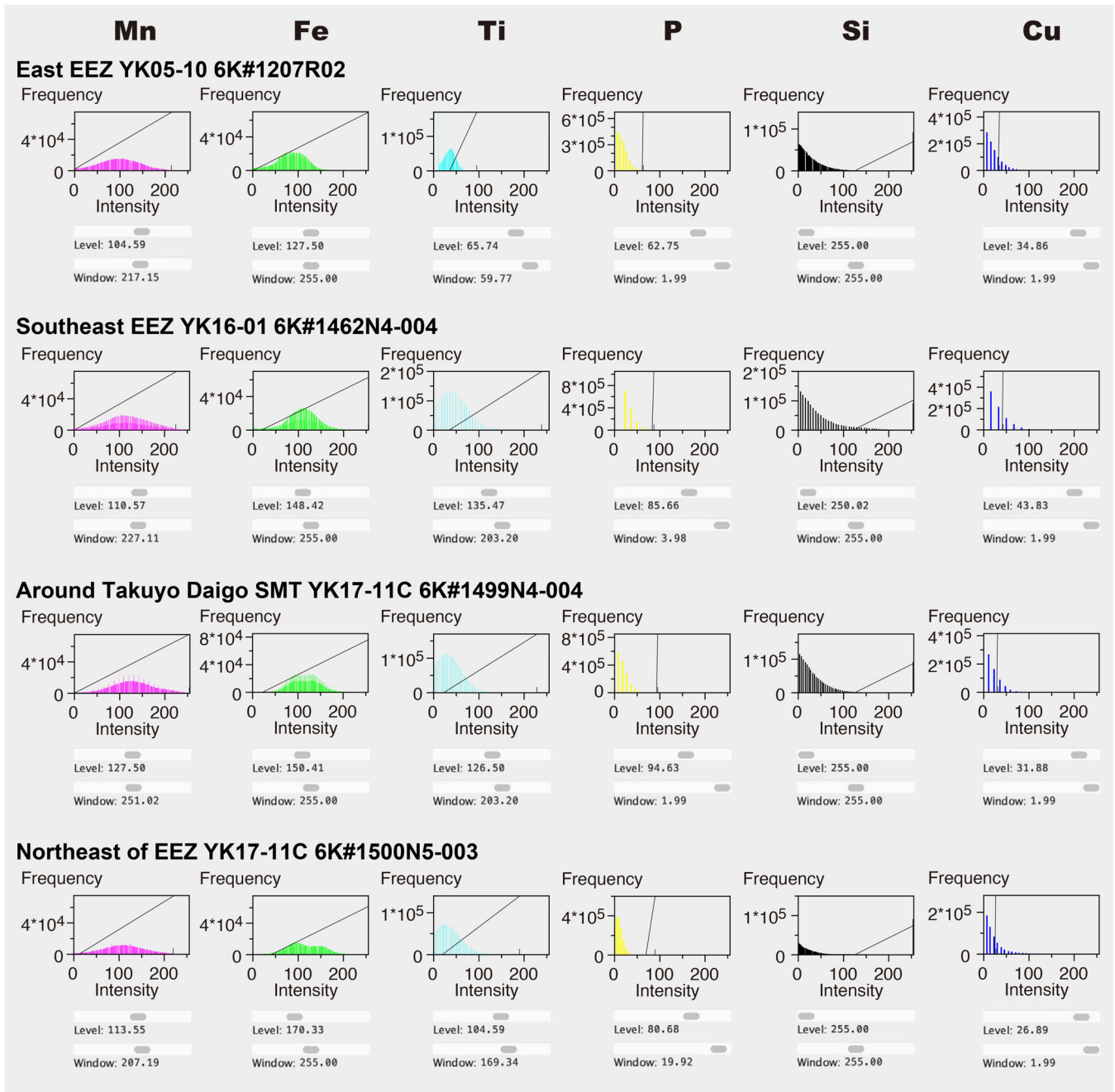


**FIGURE 5** Intensity histograms of representative samples for Mn, Fe, Ti, P, Si, and Cu for each region. The “window” indicates a range of minimum and maximum. The “level” indicates the position of that range in the intensity space. Black lines connect values of minimum and maximum, showing the results of level adjustment for each element in the merged image (see text for details)

YK05-10#1207R02

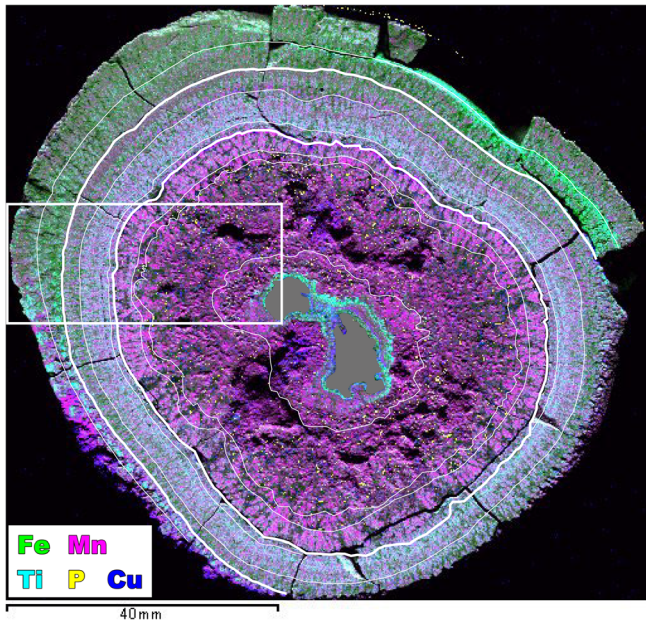


**FIGURE 6** Merged multichemical feature map of sample 6K#1207R02 from the East EEZ region. The strategy used to create this map by merging of Mn, Fe, Ti, P, Si, and Cu, and the colors used for each element are discussed in Section 5.2 of the main text. The intensity of the Si is minimized to improve the visualization of the fundamental features of the Fe–Mn oxide layers. The thick white lines indicate the boundaries of the layers L0, L1, and L2, and the thin white lines indicate the sublayer boundaries of each layer. The white box indicates the area shown in Figure 7. The gray field indicates the nuclei of this sample

entire Fe–Mn oxide of nodule. In contrast, the inner and outer rims of L1 exhibited a slightly increased Si intensity owing to the increasing abundance of sediment fill. We thus subdivided the layer L1 into L1 Inner, L1 Middle, and L1 Outer. The layer L1 Inner is distinguished by having lower Fe than the outer two sublayers, corresponding to a growth section of columnar  $\delta$ -MnO<sub>2</sub>. The inner part of L2 (around the nuclei) is characterized by having lower Si than the other L2 sublayers. The abundance of BCP particles drastically decreases just inside the boundary of the layers L2 and L1. Independent of these two observations, the texture of the Fe changes from massive to layered in the middle part of L2. Therefore, we defined the layers as L2 Inner, L2 Middle, L2 Outer, and L2 Outermost. Although the layers L2 Middle and L2 Outer are irregularly bounded, the critical constraint for the identification is that the layer L2 Outer was commonly composed of a few growth sections of columnar  $\delta$ -MnO<sub>2</sub>.

#### 5.4 | Chemostratigraphic correlations of the Minamitorishima EEZ nodules

A multichemical feature map of all the samples was constructed by applying the same adjustment strategy for each merged intensity channel (see Section 5.2; Figure 8); characteristics of the first-order L0 (high Fe and high Fe/Mn), L1 (high Ti), and L2 (high Mn and low Fe/Mn) layers were represented by the same coloration. As stated by Machida et al. (2016), the textural and compositional changes throughout the growth history of their nodules are similar to those of the Fe–Mn crust on large seamounts in the western Pacific

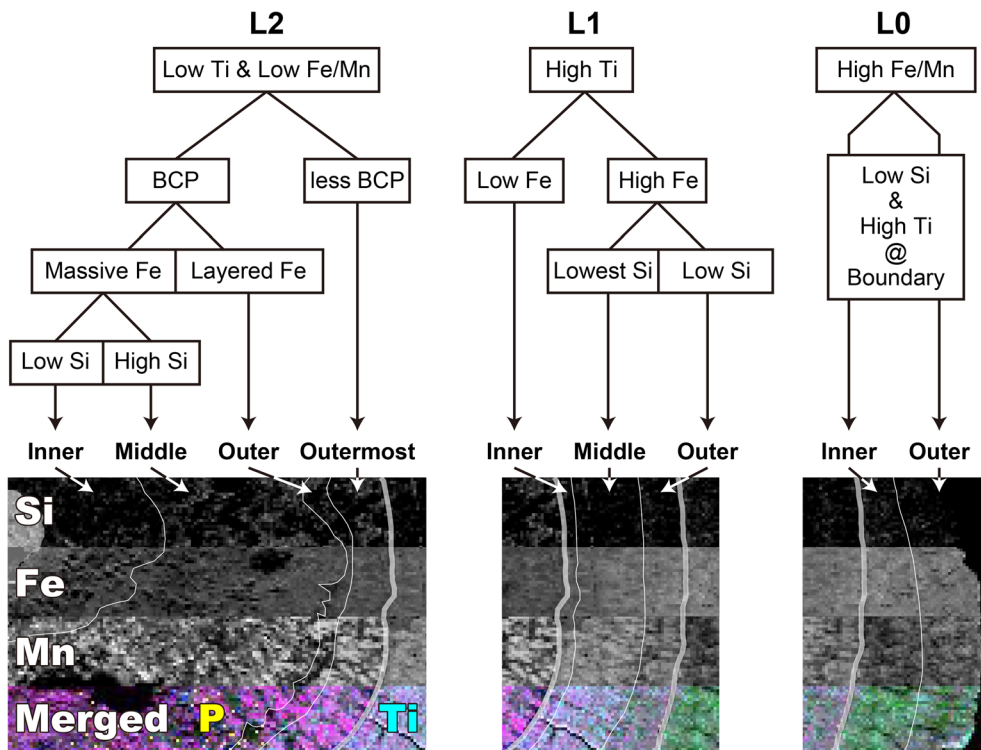
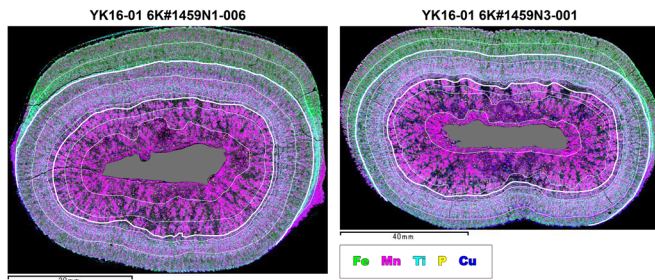
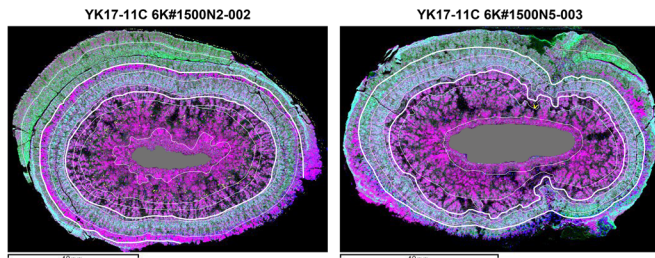


**FIGURE 7** Flowchart defining the sublayers of the ferromanganese nodule sampled from around Minamitorishima Island. The lower panel are portions of the representative compositional are of sample 6K#1207R02 from the East EEZ region, as indicated in Figure 6. The panels have been inverted to match the flowchart and are separated into four areas: Si, Fe, Mn, and merged. BCP, biogenic calcium phosphates

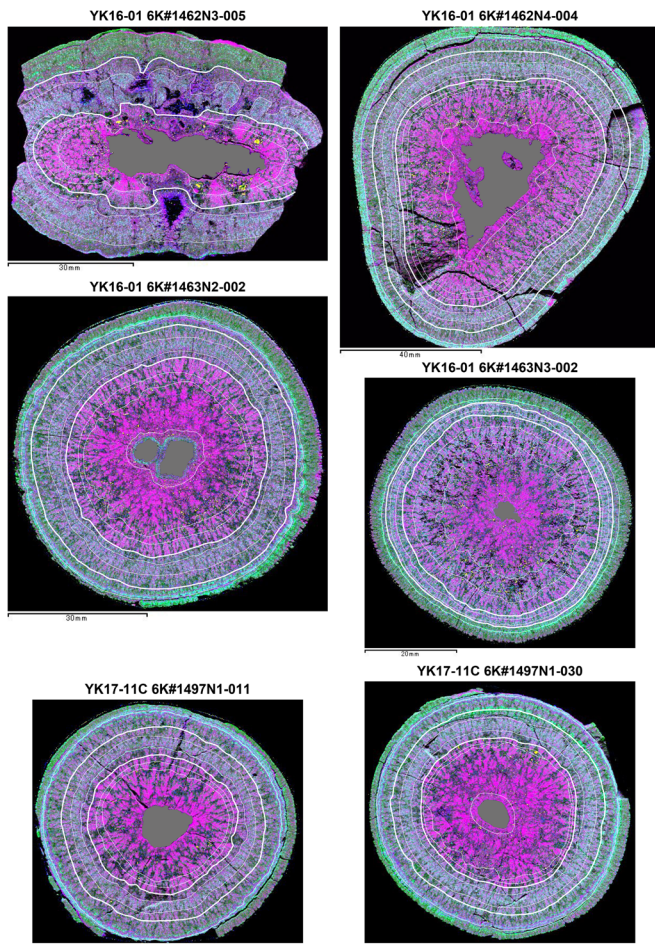
## East EEZ



## Northeast of EEZ



## Southeast EEZ



## Around Takyo Daigo SMT

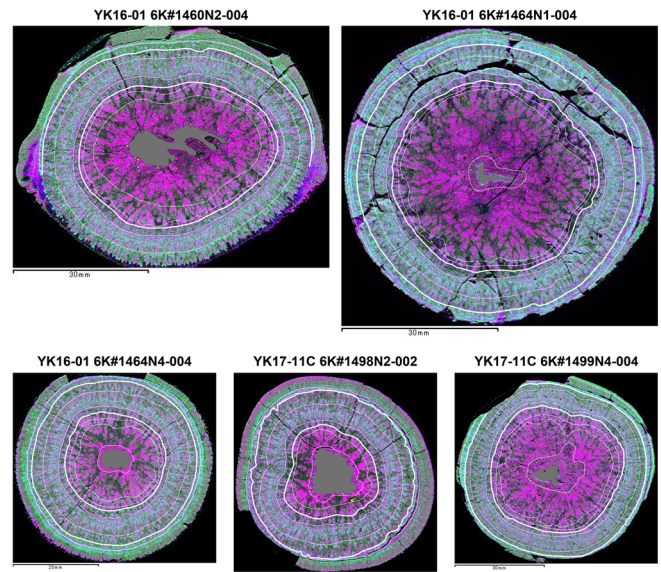


FIGURE 8 (Continued)

(Kim et al., 2005, 2006; Pan et al., 2005), the Takuyo Daigo Seamount (Nozaki et al., 2016), and petit-spot volcanoes (Azami et al., 2018). Therefore, we consider that our multichemical feature map solely visualizes a hydrogenetic Fe–Mn-(oxyhydr)oxide precipitation process, which had formed the Fe–Mn nodules and crusts.

In this study, compositional map data were obtained for the nodules collected from different geographic and geological backgrounds around Minamitorishima Island. It was expected that local problems caused by different geomorphological and geological backgrounds may be responsible for the formation of specific layer structures for each locality. However, this is not the case, and the fact that the same structure is found in all of nodules and crusts leads to the following geological implications. The important aspects are that a common deep-sea water mass had contributed to the formation of hydrogenous nodules and crust, and a common water-mass transformation history was recorded as the compositional change of Fe–Mn oxides which are distributed across the wide area in western Pacific. Structure change of Fe from L2 Middle (massive) to L2 Outer (layered) may reflect variation in precipitation process. Drastic decrease in the abundance of BCP particles between L2 Outer and Outermost layers suggest reduction of biological productivity in western Pacific. Future investigation of the growth history is required on the basis of detailed compositional and isotopic analysis including age determination for each layer.

In addition to these common chemostratigraphic features, we also recognized a regional variation, particularly in the lack of a Fe–Mn oxide sublayer(s), that had affected the size of the nodules (Figure 8). The lack of sublayer(s) was categorized as either completely missing, an extremely thin layer, or missing from one side. The completely missing category is rare, and the most often missing sublayer is the layer L2 Inner, as observed in sample 6K#1459N1-006 from the East EEZ region, sample 6K#1500N2-002 from the Northeast of EEZ region, and

**FIGURE 8** Merged multichemical feature map for all the samples analyzed in this study. In each map, the thick white lines indicate the boundaries of the layers L0, L1, and L2, and the thin white lines indicate the sublayer boundaries of each layer. The gray field indicates the nuclei of this sample

sample 6K#1463N3-002 and 6K#1467N1-011 from the Southeast EEZ region. This indicates that nuclei of the L2 Inner layer-missing samples were supplied later than for the samples with a layer L2 Inner.

The most remarkable example of the thin sublayer category was observed in the layer L0 of the samples from the Southeast EEZ (except for those from the site 6K#1462) and Around Takuyo Daigo Seamount regions (Figure 8). Although we observed that both the layer L0 Inner and the L0 Outer were thinned, this was not observed in all samples. The case missing-from-one-side category was only randomly observed. Therefore, we consider that the hiatus in Fe–Mn precipitation can be regulated on the basis of the local geomorphological and geological backgrounds. Future investigation of the cause of the hiatus in Fe–Mn precipitation is required using  $\mu$ -XRF mapping analysis that focuses especially on smaller samples. The layer L1 is present in all the samples collected from all the regions, and the layer thickness is almost the same, except for a few of the smaller nodules, such as the sample 6K#1463N3-002. As discussed by Machida et al. (2016), a massive layer (L1) is commonly observed in hydrogenous Fe–Mn crust on large seamounts in the Prime Crust Zone. Therefore, the layer L1 would be key to investigate stratigraphy and the presence or absence of hiatus of Fe–Mn oxides between different regions in the western Pacific in the future study.

## 6 | CONCLUSION

To investigate the fine-scale chemostratigraphic growth history of Fe–Mn nodules from the Minamitorishima EEZ, we conducted micro-focus X-ray mapping analysis with EDS of cross-sectioned nodules, and compared this with the compositional profile of a previously reported nodule from the eastern end of the Minamitorishima EEZ. The results led to the following conclusions:

1. A first-order concentric layer comprising layers L0, L1, and L2 are confirmed by the  $\mu$ -XRF mapping analysis. Moreover, our analysis revealed that the general pattern of compositional variation is common throughout the nodule growth process across different regions.
2. We found that the X-ray intensity could be adjusted using the same criteria for each element. Therefore, we are able to merge several compositional maps into one map visualizing multi-dimensional data. Mn, Fe, Ti, P, Si, and Cu represent the main lithological components involved in the hydrogenous Fe–Mn oxides in the Minamitorishima EEZ. Based on a merged multielemental map, the first-order concentric Fe–Mn layer was subdivided into nine sublayers exhibiting different chemical signatures.
3. Factors regulating the size of the nodules included not only differences in the size of the nuclei but also the thickness of the Fe–Mn oxide. The merged multielemental map reveal a missing sublayer in some samples owing to either a delay in the supply of nuclei or a growth hiatus in the layers L0 and L2. In contrast, it was commonly observed in all the samples that the layer L1 did not have a missing sublayer. Since the layer L1 is also recognized in Fe–Mn crust from the western Pacific, the chemostratigraphic correlation of Fe–Mn

oxides from other areas could be explored on the basis of the layer L1 as the key facies.

## ACKNOWLEDGMENTS

We gratefully acknowledge the captains, crews and shipboard scientific parties of the *R/V Yokosuka*, and operating team of the *SHINKAI 6500* for their efficient work during the cruises YK16-01, and YK17-11C. The both research cruises were conducted in the cross-ministerial Strategic Innovation Promotion Program (SIP) of Japan. We thank J. Kaneko and T. Sato for their help during the acoustic survey of the Minamitorishima EEZ. Topographic and acoustic backscatter intensity data of Northeast of EEZ region were collected during Japan's continental shelf survey project by Hydrographic and Oceanographic Department, Japan Coast Guard. Critical reviews and courteous comments by two anonymous reviewers and editorial handling by Y. Iryu and T. Tsujimori are gratefully acknowledged. The cross-ministerial SIP of Japan; JSPS through the Grant-in-Aid Scientific Research (S) No. 15H05771 and (A) No. 17H01361.

## CONFLICT OF INTEREST

The authors have no competing interests to declare.

## ORCID

Shiki Machida  <https://orcid.org/0000-0002-1069-7214>

Kentaro Nakamura  <https://orcid.org/0000-0001-9115-589X>

Tetsu Kogiso  <https://orcid.org/0000-0001-6386-9801>

Kyoko Okino  <https://orcid.org/0000-0001-7070-7982>

Yasuhiro Kato  <https://orcid.org/0000-0002-5711-8304>

## REFERENCES

- Aftabuzzaman, M. R., Yomogoda, K., Suzuki, S., Takayanagi, H., Ishigaki, A., Machida, S., Asahara, Y., Yamamoto, K., Hirano, N., Sano, S., Chiyonobu, S., Bassi, D., & Iryu, Y. (2021). Multi-approach characterization of shallow-water carbonates off Minamitorishima and their depositional settings/history. *Island Arc*, this issue.
- Aplin, A. C., & Cronan, D. S. (1985a). Ferromanganese oxide deposits from the Central Pacific Ocean. I. Encrustations from the Line Islands Archipelago. *Geochimica et Cosmochimica Acta*, 49, 427–436.
- Aplin, A. C., & Cronan, D. S. (1985b). Ferromanganese oxide deposits from the Central Pacific Ocean. II. Nodules and associated sediments. *Geochimica et Cosmochimica Acta*, 49, 437–451.
- Azami, K., Hirano, N., Machida, S., Yasukawa, K., & Kato, Y. (2018). Rare earth elements and yttrium (REY) variability with water depth in hydrogenous ferromanganese crusts. *Chemical Geology*, 493, 224–233.
- Burns, R. G., & Burns, V. M. (1979). Manganese oxides. In R. G. Burns (Ed.), *Marine minerals. Min. Soc. Am. Short Course Notes 6* (pp. 1–46).
- Calvert, S. E., & Price, N. B. (1977). Geochemical variation in ferromanganese nodules and associated sediments from the Pacific Ocean. *Marine Chemistry*, 5, 43–74.
- Fujinaga, K., Yasukawa, K., Nakamura, K., Machida, S., Takaya, Y., Ohta, J., Araki, S., Liu, H., Usami, R., Maki, R., Haraguchi, S., Nishio, Y., Usui, Y., Nozaki, T., Yamazaki, T., Ichiyama, Y., Ijiri, A., Inagaki, F., Machiyama, H., ... KR13-02, MR13-E02 Leg 2 and KR14-02 Cruise Members. (2016). Geochemistry of REY-rich mud in the Japanese Exclusive Economic Zone around Minamitorishima Island. *Geochemical Journal*, 50, 575–590.
- Hein, J. R., Conrad, T. A., & Dunham, R. E. (2009). Seamount characteristics and mine-site model applied to exploration and mining-lease-block selection for cobalt-rich ferromanganese crusts. *Marine Georesources &*

- Geotechnology*, 27, 160–176. <https://doi.org/10.1080/10641190902852485>
- Hein, J. R., Koschinsky, A., & Kuhn, T. (2020). Deep-ocean polymetallic nodules as a resource for critical materials. *Nature Reviews Earth & Environment*, 1, 158–169.
- Hein, J. R., Mizell, K., Koschinsky, A., & Conrad, T. A. (2013). Deep-ocean mineral deposits as a source of critical metals for High-tech green-technology applications: Comparison with land-based resources. *Ore Geology Reviews*, 51, 1–14. <https://doi.org/10.1016/j.oregeorev.2012.12.001>
- Hirano, N., Sumino, H., Morishita, T., Machida, S., Kawano, T., Yasukawa, K., Hirata, T., Kato, Y., & Ishii, T. (2021). An Paleogene magmatic overprint on Cretaceous seamounts of the western Pacific. *Island Arc*, 30(1).
- Iijima, K., Yasukawa, K., Fujinaga, K., Nakamura, K., Machida, S., Takaya, Y., Ohta, J., Haraguchi, S., Nishio, Y., Usui, Y., Nozaki, T., Yamazaki, T., Ichiyama, Y., Ijiri, A., Inagaki, F., Machiyama, H., Suzuki, K., Kato, Y., & KR13-02 Cruise Members. (2016). Discovery of extremely REY-rich mud in the western North Pacific Ocean. *Geochemical Journal*, 50, 557–573.
- Kashiwabara, T., Oishi, Y., Sakaguchi, A., Sugiyama, T., Usui, A., & Takahashi, Y. (2014). Chemical processes for the extreme enrichment of tellurium into marine ferromanganese oxides. *Geochimica et Cosmochimica Acta*, 131, 150–163.
- Kashiwabara, T., Toda, R., Fujinaga, K., Honma, T., Takahashi, Y., & Kato, Y. (2014). Determination of host phase of lanthanum in deep-sea REY-rich mud by XAFS and  $\mu$ -XRF using high-energy synchrotron radiation. *Chemistry Letters*, 43, 199–200.
- Kashiwabara, T., Toda, R., Nakamura, K., Yasukawa, K., Fujinaga, K., Kubo, S., Nozaki, T., Takahashi, Y., Suzuki, K., & Kato, Y. (2018). Synchrotron X-ray spectroscopic perspective on the formation mechanism of REY-rich muds in the Pacific Ocean. *Geochimica et Cosmochimica Acta*, 240, 274–292.
- Kato, Y., Fujinaga, K., Nakamura, K., Takaya, Y., Kitamura, K., Ohta, J., Toda, R., Nakashima, T., & Iwamori, H. (2011). Deep-sea mud in the Pacific Ocean as a potential resource for rare-earth elements. *Nature Geoscience*, 4, 535–539.
- Kim, J., Hyeong, K., Jung, H.-S., Moon, J.-W., Kim, K.-H., & Lee, I. (2006). Southward shift of the Intertropical Convergence Zone in the western Pacific during the late Tertiary: Evidence from ferromanganese crusts on seamounts west of the Marshall Islands. *Paleoceanography*, 21, PA4218.
- Kim, J., Hyeong, K., Yoo, C. M., Moon, J. W., Kim, K. H., Ko, Y. T., & Lee, I. (2005). Textural and geochemical characteristics of Fe-Mn crusts from four seamounts near the Marshall Islands, western Pacific. *Geosciences Journal*, 9, 331–338.
- Koppers, A. A., Staudigel, H., Pringle, M. S., & Wijbrans, J. R. (2003). Short-lived and discontinuous intraplate volcanism in the South Pacific: Hot spots or extensional volcanism? *Geochemistry, Geophysics, Geosystems*, 4, 1–49. <https://doi.org/10.1029/2003GC000533>
- Koschinsky, A., & Halbach, P. (1995). Sequential leaching of marine ferromanganese precipitates: Genetic implications. *Geochimica et Cosmochimica Acta*, 59, 5113–5132.
- Liao, J., Sun, X., Li, D., Sa, R., Lu, Y., Lin, Z., Xu, L., Zhan, R., Pan, Y., & Xu, H. (2019). New insights into nanostructure and geochemistry of bioapatite in REE-rich deep-sea sediments: LA-ICP-MS, TEM, and Z-contrast imaging studies. *Chemical Geology*, 512, 58–68.
- Machida, S., Fujinaga, K., Ishii, T., Nakamura, K., Hirano, N., & Kato, Y. (2016). Geology and geochemistry of ferromanganese nodules in the Japanese Exclusive Economic Zone around Minamitorishima Island. *Geochemical Journal*, 50, 539–555.
- Machida, S., Sato, T., Yasukawa, K., Nakamura, K., Iijima, K., Nozaki, T., & Kato, Y. (2019). Visualisation method for the broad distribution of sea-floor ferromanganese deposits. *Marine Georesources & Geotechnology*, 39(3), 1–13. <https://doi.org/10.1080/1064119X.2019.1696432>
- Marini, C., Rovira, A. M. D., Ramanan, N., Olszewski, W., Joseph, B., & Simonelli, L. (2019). Combined micro X-ray absorption and fluorescence spectroscopy to map phases of complex systems: The case of sphalerite. *Scientific Reports*, 9, 18857.
- Müller, R. D., Sdrolias, M., Gaina, C., & Roest, W. R. (2008). Age, spreading rates, and spreading asymmetry of the world's ocean crust. *Geochemistry, Geophysics, Geosystems*, 9, Q04006. <https://doi.org/10.1029/2007GC001743>
- Nakamura, K., Machida, S., Okino, K., Masaki, Y., Iijima, K., Suzuki, K., & Kato, Y. (2016). Acoustic characterization of pelagic sediments using sub-bottom profiler data: Implications for the distribution of REY-rich mud in the Minamitorishima EEZ, western Pacific. *Geochemical Journal*, 50, 605–619.
- Nakanishi, M., Tamaki, K., & Kobayashi, K. (1989). Mesozoic magnetic anomaly lineations and seafloor spreading history of the Northwestern Pacific. *Journal of Geophysical Research*, 94, 15437–15462.
- Nozaki, T., Tokumaru, A., Takaya, Y., Kato, Y., Suzuki, K., & Urabe, T. (2016). Major and trace element compositions and resource potential of ferromanganese crust at Takuyo Daigo Seamount, northwestern Pacific Ocean. *Geochemical Journal*, 50, 527–537.
- Ohta, J., Yasukawa, K., Machida, S., Fujinaga, K., Nakamura, K., Takaya, Y., Iijima, K., Suzuki, K., & Kato, Y. (2016). Geological factors responsible for REY-rich mud in the western North Pacific Ocean: Implications from mineralogy and grain size distributions. *Geochemical Journal*, 50, 591–603.
- Ohta, J., Yasukawa, K., Nozaki, T., Takaya, Y., Mimura, K., Fujinaga, K., Nakamura, K., Usui, Y., Kimura, J.-I., Chang, Q., & Kato, Y. (2020). Fish proliferation and rare-earth deposition by topographically induced upwelling at the late Eocene cooling event. *Scientific Reports*, 10, 9896.
- Oikawa, M., & Morishita, T. (2009). Submarine topography in the east sea to the Minami-Tori Shima Island, Northwest Pacific Ocean. *Report of Hydrographic and Oceanographic Researches*, 45, 13–22 (in Japanese with English abstract).
- Pan, J., De Carlo, E. H., Yang, Y., Liu, S., & You, G. (2005). Effect of phosphatization on element concentration of cobalt-rich ferromanganese crusts. *Acta Geologica Sinica*, 79, 349–355.
- Petersen, S., Krättschell, A., Augustin, N., Jamieson, J., Hein, J. R., & Hannington, M. D. (2016). News from the seabed – Geological characteristics and resource potential of deep-sea mineral resources. *Marine Policy*, 70, 175–187.
- Sager, W. W., Duncan, R. A., & Handschumacher, D. W. (1993). Paleomagnetism of the Japanese and Marcus-Wake seamounts, western Pacific ocean. In M. S. Pringle, W. W. Sager, W. V. Sliter, & S. Stein (Eds.), *The Mesozoic Pacific: Geology, tectonics, and volcanism. AGU geophysical monograph* (Vol. 77, pp. 401–435). Washington, DC: American Geophysical Union.
- Shimomura, R., Nakamura, K., Machida, S., Yasukawa, K., Fujinaga, K., & Kato, Y. (2018). Elucidation of the growth history of Fe-Mn nodules in the Western North Pacific Ocean using X-ray CT and elemental mapping. *Goldschmidt Abstracts*, 2329.
- Sipos, P., Balázs, R., Bozsó, G., & Németh, T. (2016). Changes in microfabric and re-distribution of Fe and Mn with nodule formation in a floodplain soil. *Journal of Soils and Sediments*, 16, 2105–2117.
- Takaya, Y., Yasukawa, K., Kawasaki, T., Fujinaga, K., Ohta, J., Usui, Y., Nakamura, K., Kimura, J.-I., Chang, Q., Hamada, M., Dodbibba, G., Nozaki, T., Iijima, K., Morisawa, T., Kuwahara, T., Ishida, Y., Ichimura, T., Kitazume, M., Fujita, T., & Kato, Y. (2018). The tremendous potential of deep-sea mud as a source of rare-earth elements. *Scientific Reports*, 8, 5763.
- Tharalson, E. R., Monecke, T., Reynolds, T. J., Zeeck, L., Pfaff, K., & Kelly, N. M. (2019). The distribution of precious metals in high-grade banded quartz veins from low-sulfidation epithermal deposits: Constraints from  $\mu$ XRF mapping. *Minerals*, 9, 740.
- Usui, A., Nishi, K., Sato, H., Nakasato, Y., Thornton, B., Kashiwabara, T., Tokumaru, A., Sakaguchi, A., Yamaoka, K., Kato, S., Nitahara, S., Suzuki, K., Iijima, K., & Urabe, T. (2017). Continuous growth of hydrogenetic ferromanganese crusts since 17 Myr ago on Takuyo-Daigo Seamount, NW Pacific, at water depths of 800–5500 m. *Ore Geology Reviews*, 87, 71–87.

Yasukawa, K., Liu, H., Fujinaga, K., Machida, S., Haraguchi, S., Ishii, T., Nakamura, K., & Kato, Y. (2014). Geochemistry and mineralogy of REY-rich mud in the eastern Indian Ocean. *Journal of Asian Earth Sciences*, 93, 25–36.

#### SUPPORTING INFORMATION

Additional supporting information may be found online in the Supporting Information section at the end of this article.

**How to cite this article:** Machida S, Nakamura K, Kogiso T, et al. Fine-scale chemostratigraphy of cross-sectioned hydrogenous ferromanganese nodules from the western North Pacific. *Island Arc*. 2021;30:e12395. <https://doi.org/10.1111/iar.12395>